Wind Resistant Transition Trajectory Generation of VTOL Aircraft under Control Allocation Framework

Gao Lou [*] and Molong Duan [†]
Hong Kong University of Science and Technology, Hong Kong, China

Yu Liang[‡]
Beihang University, Beijing, China

Xiaowen Shan [§]
Southern University of Science and Technology, Shenzhen, China

The vertical-takeoff-and-landing (VTOL) suffers from gusts and disturbances when switching between hovering and level flight. The drastic dynamic change may introduce low stability margins and cause instability. The transition trajectory plays a vital role in the process and thus needs to be optimized. In this work, a wind resistant transition trajectory generation method for VTOL aircraft is proposed. The transition trajectory generation exploits the control allocation framework and defines a unique control overflow region based on the trajectory and disturbance conditions. The wind resistance optimization is converted to a minimization of the modulated overflow region and thus is solvable in a conventional optimal control framework. A B-spline parameterization is also introduced to alleviate the computational load. The proposed transition trajectory generation methods have been verified in simulation with an ETS-20 VTOL aircraft model and Von Karman gust profile. Enhanced wind resistance is observed in comparison to other representative transition trajectories.

I. Introduction

Vertical takeoff and landing (VTOL) aircraft are characterized by their vertical takeoff and landing capabilities [1]which enable the aircraft to operate from a wider range of locations without requiring runway infrastructure while maintaining the capability of efficient long-distance level flight [2]. They typically begin the mission with a vertical takeoff, similar to quadrotor drones, and gradually transition to level flight. However, the stability of VTOL aircraft dynamics is highly susceptible to disturbances, particularly during the transition, primarily due to the complexity of their design and the interactions between their propellers and lift-generating structures [3,4].

The stability of VTOL aircraft is the core focus of existing investigations. Takaaki et al. [5] proposed a stability augmentation method for VTOL aircraft, with an emphasis on the hovering phase, but the method may be limited in extending to all flight phases and their transitions. Li et al. [3] and Yang et al. [4] developed a robust controller for aircraft transition and stability analysis. However, these methods are based on the extension of linear controllers and are limited in evaluating the gust rejection capability due to the actuator and its rate saturations. In the control allocation framework, the concepts of the attainable subset method [6] shed light on this problem and are promising in evaluating and further optimizing the gust rejection capability.

Following the controller optimization, the transition trajectory optimization is a critical aspect in VTOL research. Banazadeh et al. [7] proposed to minimize transition phase durations and focused on the influence of the thrust-to-

---

[*] Research assistant, Department of Mechanical and Aerospace Engineering.

[†] Assistant professor, Department of Mechanical and Aerospace Engineering, corresponding author (duan@ust.hk), AIAA Member.

[‡] Associate Researcher, Unmanned Systems Research Institute.

[§] Chair Professor, Department of Mechanics and Aerospace Engineering.

weight ratio on transition; their work highlights that the ratio plays a critical role in determining the efficiency and stability of the VTOL during its transition phase. Their another work [8] considered stall angle in optimization, which is more complex in aircraft with front-positioned propellers. This approach underscores the complexity and multifaceted nature of trajectory optimization in VTOL aircraft, where multiple factors must be balanced to achieve optimal performance. Verling et al. [9] primarily focused on developing an attitude control system on SO3 for a flying-wing tail sitter UAV, applicable across all attitude configurations and operating modes. Additionally, they investigated constant-altitude reverse transitions (from cruise to hover), noting that optimal trajectories involve significant altitude variation. Naldi and Marconi [10] focused on minimizing the transition endurance and energy consumption in VTOL aircraft. They approached this by dividing the problem into two single-objective optimization problems. Their focus on minimizing energy consumption and transition time is particularly relevant in the context of efficient and sustainable VTOL operation. While previous studies have significantly advanced the optimization of transition trajectories in VTOL aircraft, there remains a notable research gap in comprehensively integrating the impact of aerodynamic disturbances into the optimization process. The optimization of VTOL aircraft trajectories under disturbance conditions presents unique challenges, as these disturbances can significantly affect the stability and control of the aircraft. Therefore, there is a need for further research that explores advanced trajectory generation methods that can effectively account for and mitigate the impact of these disturbances. This research aims to bridge this gap by proposing a method that directly incorporates disturbance models into the trajectory optimization process, thereby enhancing the disturbance rejection capabilities of VTOL aircraft and ensuring more reliable and stable flight under varying environmental conditions.

In this paper, we aim to enhance VTOL aircraft transition by exploring their wind resistance capabilities and devising effective trajectory optimization methods within the control allocation framework. This includes defining stability and developing quantitative stability measures, which are integrated into trajectory optimization to enhance disturbance rejection in flight. The general VTOL aircraft model is defined and the trajectory generation approach using the control allocation and overflow region is detailed in Section II. The method is verified in simulation with a tail-sitter VTOL aircraft ETS-20 under different levels of Von Karman gusts in Section III, followed by the conclusions in Section IV.

II.　Wind Resistant VTOL Aircraft Transition Trajectory Optimization

A. General VTOL Aircraft Dynamics and Control Allocation Enabled Overflow Region

Consider an m degree-of-freedom nonlinear VTOL controlled with n actuators. Its aircraft dynamics under control allocation framework, given by

$$\begin{cases} \dot{\boldsymbol{x}} = f(\boldsymbol{x}, \boldsymbol{u}), \\ \boldsymbol{u} = g(\boldsymbol{x}, \boldsymbol{\delta}), \\ \dot{\boldsymbol{\delta}} \in [\bar{\boldsymbol{\nu}}, \underline{\boldsymbol{\nu}}], \\ \boldsymbol{\delta} \in [\bar{\boldsymbol{\delta}}, \underline{\boldsymbol{\delta}}], \end{cases} \tag{1}$$

where $\boldsymbol{x} \in \mathbb{R}^m$ refers to the aircraft motion states including translational and rotational velocity, $\boldsymbol{u} \in \mathbb{R}^m$ refers to the generalized force (e.g., force and moment) of the aircraft experienced. The generalized force is assumed to be statically and nonlinearly connected to the actuator input $\boldsymbol{\delta} \in \mathbb{R}^n$, which is a combination of all control surface deflections, propeller speeds, and thruster forces. The actuator input's value and time-domain changing rate are bounded by $[\bar{\boldsymbol{\delta}}, \underline{\boldsymbol{\delta}}]$ and $[\bar{\boldsymbol{\nu}}, \underline{\boldsymbol{\nu}}]$, respectively. This control allocation framework is widely adopted in modern aircraft system for its enhanced convenience in handling over-actuated systems to enhance the fault tolerance of the system [11]. It also benefits VTOL aircraft modeling and control as it unified the control of different types of actuators under a common

framework. The function f represents the equation of motion (EOM), while g corresponds to the aerodynamic forces' detailed contributions.

For further discussion of the trajectory optimization and simulation, the system given in Eq. (1) is discretized and it is assumed that the local control effectiveness is dependent on the aircraft state. The aerodynamic equation g is thus converted to a local linear-parameter-varying (LPV) framework such that the control effectiveness can be conveniently evaluated. The discrete dynamics is given by

$$
\begin{cases}
\boldsymbol{x}_{i+1} = \boldsymbol{x}_i + f(\boldsymbol{x}_i, \boldsymbol{u}_i)\, \Delta t, \\
\boldsymbol{u}_{i+1} = \boldsymbol{u}_i + \Delta \boldsymbol{u}_i, \\
\Delta \boldsymbol{u}_i = B(\boldsymbol{x}_i, \boldsymbol{\delta}_i)\, \Delta \boldsymbol{\delta}_i, \\
B(\boldsymbol{x}_i, \boldsymbol{\delta}_i) = \dfrac{\partial g(\boldsymbol{x}_i, \boldsymbol{\delta}_i)}{\partial \boldsymbol{\delta}}, \\
\boldsymbol{\delta}_{i+1} = \boldsymbol{\delta}_i + \Delta \boldsymbol{\delta}_i,
\end{cases}
\tag{2}
$$

where $B(\boldsymbol{x}_i, \boldsymbol{\delta}_i) \in \mathbb{R}^{m \times n}$ refers to the linear control effective matrix of the VTOL aircraft, $\boldsymbol{x}_i$, $\boldsymbol{u}_i$ and $\boldsymbol{\delta}_i$ denote the states, aircraft moments and forces, and actuator inputs at the time step i. The actuator input's bounds in its value and speed are also converted to the discrete formulations, given by

$$
\begin{cases}
\Delta \delta_{ij} \in \left[\Delta \underline{\delta}_{ij}, \Delta \overline{\delta}_{ij} \right], \quad j = 1, ..., n, \\
\Delta \overline{\delta}_{ij} = \min\{ \overline{\nu}_j \Delta t, \overline{\delta}_j - \delta_{ij} \}, \\
\Delta \underline{\delta}_{ij} = \max\{ \underline{\nu}_j \Delta t, \underline{\delta}_j - \delta_{ij} \}.
\end{cases}
\tag{3}
$$

In this control allocation framework, the required generalized forces typically can be calculated given the aircraft trajectory. This inverse relationship is exploited in this work to calculate the required generalized force of a given reference trajectory. Consider the VTOL aircraft state tracks a given desirable state trajectory $\boldsymbol{x}_\mathrm{d}(t)$ perfectly. To achieve this perfect tracking, the required ideal generalized force in discrete time is given by

$$
\boldsymbol{u}_{\mathrm{d},i} = \gamma(\boldsymbol{x}_{\mathrm{d},i}, \boldsymbol{x}_{\mathrm{d},i-1}).
\tag{4}
$$

This ideal control input $\boldsymbol{u}_{\mathrm{d},i}$ is further used for calculating its increment $\Delta \boldsymbol{u}_{\mathrm{d},i}$. According to Eq. (2), the relationship between the $\Delta \boldsymbol{u}_i$ and $\Delta \boldsymbol{\delta}_i$ is locally linear, indicating that generating $\Delta \boldsymbol{u}_{\mathrm{d},i}$ via aerodynamics requires finding an appropriate $\Delta \boldsymbol{\delta}_{\mathrm{d},i}$ through control allocation with the local control effectiveness matrix. This control allocation process is a local linear programming (LP) process [12], and it is assumed to be solvable in the format with a slack variable $\boldsymbol{s}$, given by

$$
\begin{cases}
B\boldsymbol{\varepsilon} - \boldsymbol{s} \leqslant \Delta \boldsymbol{u}_{\mathrm{d},i} - B\Delta \underline{\boldsymbol{\delta}}_i, \\
-B\boldsymbol{\varepsilon} - \boldsymbol{s} \leqslant -\Delta \boldsymbol{u}_{\mathrm{d},i} + B\Delta \underline{\boldsymbol{\delta}}_i, \\
\boldsymbol{\varepsilon} \leqslant \Delta \overline{\boldsymbol{\delta}}_i - \Delta \underline{\boldsymbol{\delta}}_i.
\end{cases}
\tag{5}
$$

where $\boldsymbol{\varepsilon} = \Delta \boldsymbol{\delta}_{\mathrm{d},i} - \Delta \underline{\boldsymbol{\delta}}_i$ is the actuator deviation from its lower bounds at ith time step. The linear programming objective is to minimize the slack variable $\boldsymbol{s}$. With the constraint of $\boldsymbol{\varepsilon}$, the search region of $\Delta \boldsymbol{\delta}_{\mathrm{d},i}$ is limited. With the constraints on $\Delta \boldsymbol{\delta}_{\mathrm{d},i}$, the achievable sets (at ith time step) in the actuator space and in the generalized force space are defined as D_i and U_i, respectively. They are given by

$$
\begin{cases}
D_i = \left\{ \Delta \boldsymbol{\delta}_{\mathrm{d},i} \in \mathbb{R}^n \,\middle|\, \Delta \underline{\delta}_{ij} \leqslant \Delta \delta_{dij} \leqslant \Delta \overline{\delta}_{ij}, \ j = 1, ..., n \right\}, \\
U_i = \left\{ \Delta \boldsymbol{u}_{\mathrm{a},i} \in \mathbb{R}^m \,\middle|\, \Delta \boldsymbol{u}_{\mathrm{a},i} = B\Delta \boldsymbol{\delta}_{\mathrm{d},i}, \ \Delta \boldsymbol{\delta}_{\mathrm{d},i} \in D_i \right\}.
\end{cases}
\tag{6}
$$

The calculation of all attainable $\Delta \boldsymbol{u}_{\mathrm{a},i}$ from $\Delta \boldsymbol{\delta}_{\mathrm{d},i}$ is similar to the attainable moment subset calculation in [12]. If the ideal control input $\Delta \boldsymbol{u}_{\mathrm{d},i}$ lies outside of U_i, the aircraft fails to find a suitable $\Delta \boldsymbol{\delta}_{\mathrm{d},i}$ in D_i to fulfill

$\Delta \boldsymbol{u}_{\mathrm{a},i} = \Delta \boldsymbol{u}_{\mathrm{d},i}$, indicating that the desired maneuver unachievable. In practical operations, this mismatch of attainable generalized force $\Delta \boldsymbol{u}_{\mathrm{a},i}$ and the desirable force $\Delta \boldsymbol{u}_{\mathrm{d},i}$ occurs frequently, particularly under gust and turbulences. This mismatch can cause severe consequences to the aircraft stability as it indicates that desirable motion cannot be achieved. Therefore, for aircraft stability, it is desirable to enlarge the space of U_i to reduce the probability of the potential mismatch. Also, it sheds light on the trajectory generation and optimization: it should produce a reference trajectory $\boldsymbol{x}_{\mathrm{d}}(t)$ whose corresponding ideal control input $\Delta \boldsymbol{u}_{\mathrm{d},i}$ should be either close to or within U_i.

Exploiting the attainable generalized force definition, we can define a metric highlighting the potential mismatch between the $\Delta \boldsymbol{u}_{\mathrm{d},i}$ and U_i to indirectly link to instability. For this purpose, consider the $\Delta \boldsymbol{u}_{\mathrm{a},i}$'s individual components at ith time step, is attainable magnitude is given by

$$\begin{cases} \Delta \underline{u}_{\mathrm{a},ik} = \inf\{\Delta u_{\mathrm{a},ik} \,|\, \Delta \boldsymbol{u}_{\mathrm{a},i} \in U_i\}, \\ \Delta \bar{u}_{\mathrm{a},ik} = \sup\{\Delta u_{\mathrm{a},ik} \,|\, \Delta \boldsymbol{u}_{\mathrm{a},i} \in U_i\}, \\ l_{ik} = \Delta \bar{u}_{\mathrm{a},ik} - \Delta \underline{u}_{\mathrm{a},ik}. \end{cases} \tag{7}$$

Note that the variable l_{ik} signifies the attainable subset of $\Delta u_{\mathrm{a},ik}$, $k = 1, 2, ...m$, where a larger l_{ik} implies greater maneuverability. Moreover, considering the disturbance during the flight, the actual value of Δu_{ik} should be an arbitrary value at the neighborhood of $\Delta u_{\mathrm{d},ik}$ given by

$$\Delta u_{ik} = \Delta u_{\mathrm{d},ik} + d_{ik}, \tag{8}$$

where d_{ik} representing the shift caused by external gusts. For the component $\Delta u_{\mathrm{d},ik}$, it should stay inside the l_{ik} as well as keeping more neighborhood enclosed by this region to make sure Δu_{ik} still stay inside the attainable subset after influenced by the disturbance. Assume $d_{ik} \in [\underline{d}_{ik}, \bar{d}_{ik}]$, arrange l_{ik}, $\Delta u_{\mathrm{d},ik}$, $\underline{d}_{ik}$ and $\bar{d}_{ik}$ are illustrated in Fig. 1. The green region is $[\Delta \underline{u}_{\mathrm{a},ik}, \Delta \bar{u}_{\mathrm{a},ik}]$, while the margin (red region) is formulated by $\Delta u_{\mathrm{d},ik} + \bar{d}_{ik}$ and $\Delta u_{\mathrm{d},ik} + \underline{d}_{ik}$. With these relationship, the overflow region that is out of the attainable subset is defined as

$$O_{ik} = \max\Big\{\max\big\{\Delta u_{\mathrm{d},ik} + \bar{d}_{ik} - \Delta \bar{u}_{\mathrm{a},ik}, 0\big\}, \max\big\{\Delta u_{\mathrm{d},ik} - \Delta \underline{u}_{\mathrm{a},ik} - \underline{d}_{ik}, 0\big\}\Big\}. \tag{9}$$

This term denotes the maximum generalized force gap at step i caused by the disturbance d_{ik}.
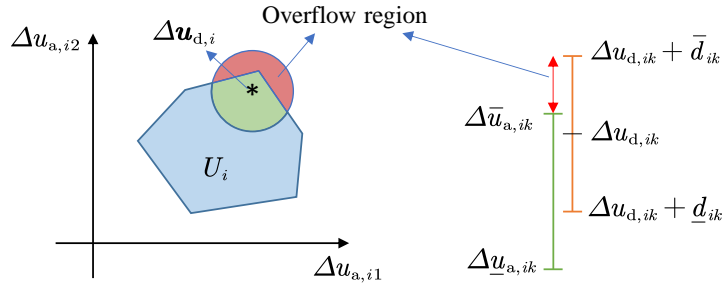
Fig. 1 Margin and attainable subset of input increment

B. Wind resistant transition trajectory generation as an optimization problem

The VTOL aircraft transition trajectory is known to be affected by gust and disturbances and is thus prone to instability. Despite the fact that the overflow region established in Eq. (9) is an indicator of the aircraft demanding generalized force out of its bound, transient overflow values are typically acceptable. Therefore, to penalize the continuous deviation of the demanded force from the aircraft capability, the overflow region needs to be integrated in time to indicate potential future instability. For this purpose, local linearization of the EOM is defined as

$$\Delta \dot{\boldsymbol{x}} \approx L_A \Delta \boldsymbol{x} + L_B \Delta \boldsymbol{u}, \tag{10}$$

where L_A and L_B are the local linearization coefficient matrices given by

$$L_A = \frac{\partial f}{\partial \boldsymbol{x}}\bigg|_{\boldsymbol{x}_i, \boldsymbol{u}_i}, \; L_B = \frac{\partial f}{\partial \boldsymbol{u}}\bigg|_{\boldsymbol{x}_i, \boldsymbol{u}_i}. \tag{11}$$

The lifted domain tensor for this linear system $W_{pr} \in \mathbb{R}^{m \times m}$ is defined as

$$W_{pr} = \begin{cases} e^{L_A(r-p)\Delta t} L_B \Delta t & \text{when } p \le r \\ 0 & \text{when } p > r \end{cases} \tag{12}$$

The lifted-domain tensor highlights the causality and how the current overflow region may affect the future. Define the overflow region time series with $\boldsymbol{O}_i = \{O_{i1}, O_{i2}, ..., O_{im}\}^\top$, the modulated overflow region time series is defined as

$$\boldsymbol{S}_i = \sum_{p=0}^r W_{pr} \boldsymbol{O}_{(i+p)}, \tag{13}$$

where $\boldsymbol{S}_i$ denotes the potential contribution to instability at the current time step considering the control effectiveness of the current state.

The VTOL aircraft typically will fly in hovering or level flight mode in most of its operations. The transition between the two modes is needed in takeoff, landing, and during other mission switches. The transition trajectory plays a vital role for aircraft stability. The transition trajectory optimization for wind resistance can be formulated with the proposed framework. Consider a transition from the hovering mode to the level flight mode. This defines the initial and ending state of the aircraft, given by $\boldsymbol{x}^{(H)}$ and $\boldsymbol{x}^{(L)}$ respectively. The transition trajectory generation is an optimal control problem given by

$$\min_{\boldsymbol{x}_d} J = \sum_{k=1}^m w_j \left(\sum_{i=0}^{N_t - r} S_{ik} \right)^2, \tag{14}$$

$$\text{s.t. } \boldsymbol{x}_{d0} = \boldsymbol{x}^{(H)}, \ \boldsymbol{x}_{dN} = \boldsymbol{x}^{(L)}, \ \boldsymbol{x}_d \in \Omega_x, \ N \in \Omega_N,$$

where w_j is the weight chosen to give precedence to crucial aircraft states to enhance the overall stability during transition, Ω_x and Ω_N are the admissible sets for the state and transition time steps respectively, and N_t is the total time steps for the transition.

The transition trajectory is expected to be smooth; inclusion of all the time steps into the optimization is not computationally efficient. Therefore, the transition trajectory is assumed to be parameterized with B-spline, such that only the control points of the transition trajectory reduce the computational load [13,14]. The desirable transition trajectory is defined as

$$\boldsymbol{x}_d(\xi) = \sum_{\zeta=1}^{n_c} N_{\zeta,e}(\xi) \boldsymbol{p}_{c,\zeta}, \tag{15}$$

where $\xi \in [0, 1]$ is the B-spline curve parameter corresponding to the normalized time, n_c is the number of control points, $\boldsymbol{p}_{c,\zeta}$ is the ζth control point, and $N_{\zeta,m}(\xi)$ is the ζth normalized e-order B-spline basis function defined as

$$N_{\zeta,1}(\xi) = \begin{cases} 1, & \xi_\zeta \le \xi < \xi_{\zeta+1} \\ 0, & \text{otherwise} \end{cases}, \tag{16}$$

$$N_{\zeta,e}(\xi) = \frac{(\xi - \xi_\zeta) N_{\zeta,e-1}(\xi)}{\xi_{\zeta+e-1} - \xi_\zeta} + \frac{(\xi_{\zeta+e} - \xi) N_{\zeta+1,e-1}(\xi)}{\xi_{\zeta+e} - \xi_{\zeta+1}}. \tag{17}$$

Note that ξ_i is the knot in a non-decreasing sequence of real number $\{\xi_1, \cdots, \xi_{n_c+m}\}$ called knot vector. Note that the entire transition trajectory is defined with the control points $\boldsymbol{p}_{c,1}, \boldsymbol{p}_{c,2}, ..., \boldsymbol{p}_{c,n_c}$. They are concatenated into a control point matrix $P_c \in \mathbb{R}^{n_c \times m}$ given by

$$P_c = [\boldsymbol{p}_{c,1}, \ \boldsymbol{p}_{c,2}, \ ..., \ \boldsymbol{p}_{c,n_c}]^\top. \tag{18}$$

Accordingly, the transition trajectory is written as

$$\boldsymbol{x}_d(\xi) = \mathbf{N}(\xi) P_c, \tag{19}$$

5

where $\mathbf{N}(\xi)$ is the vector combination of the set of basic functions of the B-spline. With this parameterization, the original optimization problem in Eq. (14) is converted to

$$\min_{P_c} J = \sum_{k=1}^{m} w_j \left(\sum_{i=0}^{N_t - r} S_{ik} \right)^2,$$

$$\text{s.t. } \mathbf{N}(0) P_c = \boldsymbol{x}^{(H)}, \ \mathbf{N}(1) P_c = \boldsymbol{x}^{(L)}, \ \mathbf{N}(\xi) P_c \in \Omega_x \ \forall \xi \in [0, 1] \ , \ N_t \in \Omega_N. \tag{20}$$

The overall optimization framework considering this B-spline parameterization is detailed in Fig. 2.
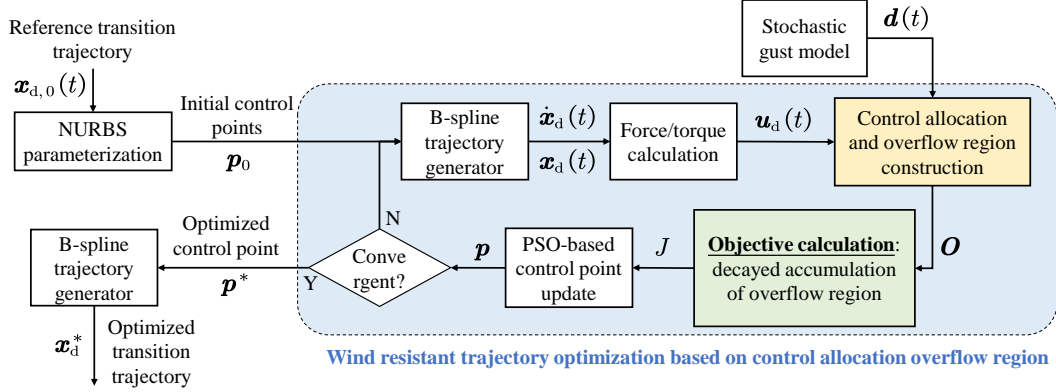
Fig. 2 Wind resistant transition trajectory optimization procedure

III. Simulation Case Study with ETS-20 VTOL Aircraft

The proposed wind resistant transition trajectory optimization based on control allocation overflow region is validated on a practical tail-sitter VTOL aircraft ETS-20 [15], as shown in Fig. 3. This aircraft is equipped with two ailerons, two V-shaped configuration elevators, two front propellers, and one vector propeller at the rear. The thrust direction of the aircraft is adjusted by a tilt motor.

(a)   (b)
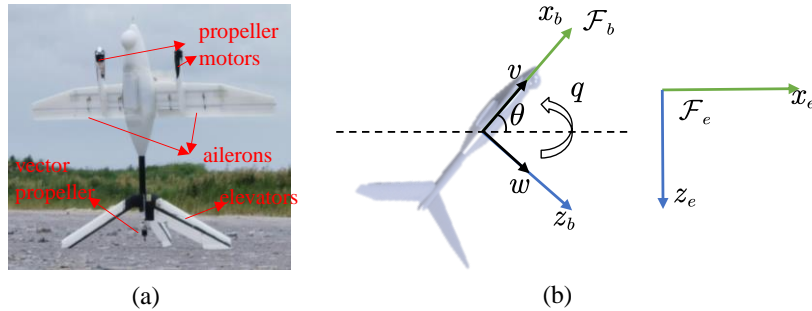
Fig. 3 Prototype ETS20 for case study (a) and the notations of states (b)

A. Aircraft dynamics modeling of ETS-20

Since the transition trajectory of this aircraft only needs to consider the longitudinal dynamics, a 3 degree-of-freedom (DOF) dynamics model has been developed for the aircraft. The aerodynamics of the model are based on a combination of wind tunnel testing, computational fluid dynamics (CFD) simulations, and force analysis. The aircraft dynamics is given by

$$\begin{cases} \dot{q} = M_y/I_{yy}, \\ \dot{v} = F_x/m - g\sin\theta - qw, \\ \dot{w} = F_z/m + g\cos\theta + qv, \\ \dot{\theta} = q, \\ \dot{h} = -v\sin\theta + w\cos\theta. \end{cases} \quad (21)$$

These equations describe the pitch angle θ, height h, velocity v and w along the x and z axes at body fixed frame $\mathcal{F}_b$, including pitch angular velocity q. The flowing equations define the moment M_y along y axis and forces F_x, F_z along x and z axes:

$$\begin{cases} M_y = T_t(v, \omega_t) l_t + M_i, \\ F_x = 2T_f(v, \omega_i) + T_t(v, \omega_t)\cos\theta_t + F_{xi}, \\ F_z = T_t(v, \omega_t)\sin\theta_t + F_{zi}, \\ \begin{bmatrix} M_i \\ F_{xi} \\ F_{zi} \end{bmatrix} = f_a(q, v, w, \delta_a, \delta_e, \omega_i, \omega_t, \theta_t). \end{cases} \quad (22)$$

where T_f and T_t are the front and rear propeller's thrust. M_i, F_{xi} and F_{zi} are the interpolation result of the database, the propeller-wing slipstream effect is shown in Fig. 4 for demonstration. While δ_a, δ_e, ω_i, ω_t and θ_t are the aileron angle, elevator angle, front propellers speed, vector propeller speed, and vector propeller tilt angle, Table 1 shows the corresponding constraints.

Table 1 Actuator physical and rate constraints of ETS-20

Actuator	Physical constraints	Rate constraints
δ_a	[-5,5] (°)	± 20 (°/s)
δ_e	[-50,50] (°)	± 50 (°/s)
ω_i	[0, 628.3] (rad/s)	± 1000 (rad/s²)
ω_t	[0,1172.9] (rad/s)	± 1000 (rad/s²)
θ_t	[-45,45] (°)	± 100 (°/s)
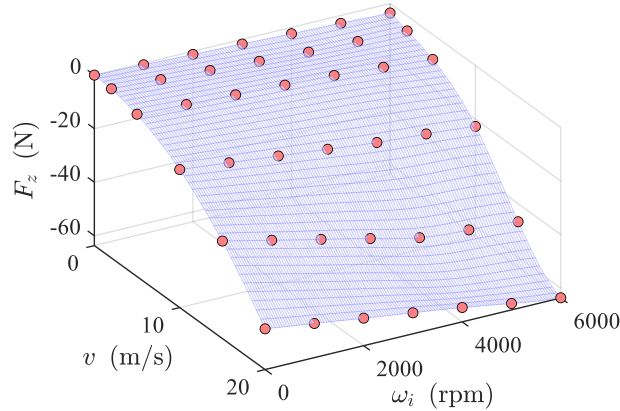
Fig. 4 Propeller-wing slipstream database

B. Wind resistant trajectory generation of ETS-20

The transition trajectory is optimized following the method detailed in Section II. The dynamics of ETS-20 in Eqs. (21) and (22) are inserted into Eq. (1), with the constraints detailed in Table 1. The constraints along the trajectory are detailed in Table 2. For the verification, Von Karman gust is introduced at the beginning of the aircraft transition phase and lasts for 35 seconds, the simulation is sustained for 70 seconds to generate the overflow region for the transition trajectory optimization. The Von Karman gust's effectiveness disturbance on the aircraft's pitch and translational velocities are shown in Fig. 5. The utmost gust speed that the aircraft can withstand within this 70-second period represents the aircraft's disturbance rejection ability.
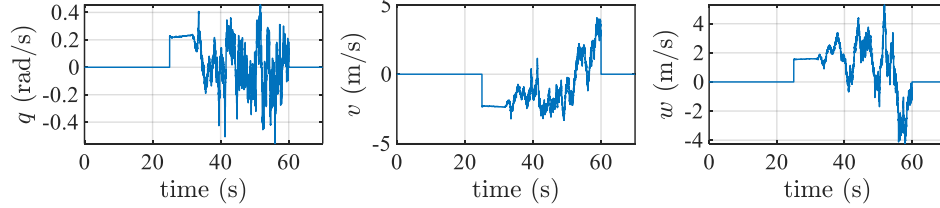
Fig. 5 Von Karman gust (24 m/s)'s effectiveness on pitch velocity q, x-axis velocity v, and z-axis velocity w

Table 2 Constraints of the trajectory

Trajectory	Initial condition	End condition	Variable region
θ_d (°)	90 (fixed)	$[0, 15]$ (free)	$[-60, 90]$
h_d (m)	-20 (fixed)	$[-100, 20]$ (free)	$[-100, 20]$
v_{ed} (m/s)	0 (fixed)	$[13, 22]$ (free)	$[0, 22]$

In the simulation, A dedicate feedback controller is designed to regulate the pitch, altitude, and ground speed of the aircraft, as shown in Fig. 6. The diagram is composed of three blocks, namely the aerodynamics and equations of motion, which calculate the aircraft behavior based on the actuator $\boldsymbol{\delta} = \{\delta_a \ \delta_e \ \omega_{pi} \ \omega_{pt} \ \theta_{pt}\}^\top$, and the backstepping control with control allocation, which together form the controller to regulate the aircraft's states $\boldsymbol{x} = \{q \ v \ w \ \theta \ h\}^\top$ and the input $\boldsymbol{u} = \{M_y \ F_x \ F_z\}^\top$. Moreover, the disturbance $\boldsymbol{d}$ in second, setup the constraints in Table 2 along the trajectory, and then apply our wind resistant trajectory optimization method, we can conduct the trajectory optimization and verification.
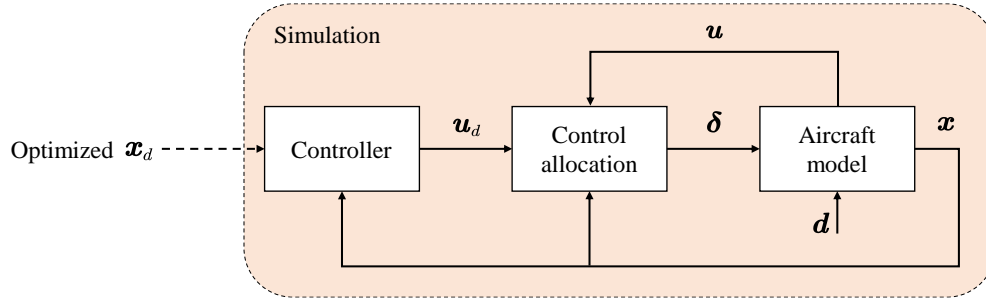
Fig. 6 Aircraft control block diagram based on backstepping control and control allocation

The control module shown in the diagram is designed for the equation of motion. Its outputs represent the desired moment and force $\boldsymbol{u}_d$ required to regulate the system's states $\boldsymbol{x}$ to the desired states, $\boldsymbol{x}_d$. The desirable control $\boldsymbol{u}_d$ is calculated as follows:

$$\begin{cases}
q_d = \dot{\theta}_d + K_1(\theta_d - \theta), \\[2pt]
w_{ed} = \dot{h}_d + K_2(h_d - h), \\[2pt]
\begin{bmatrix} v_d \\ w_d \end{bmatrix} = R_b^e \begin{bmatrix} v_{ed} \\ w_{ed} \end{bmatrix}, \\[6pt]
\begin{bmatrix} \dot{q}_r \\ \dot{v}_r \\ \dot{w}_r \end{bmatrix} = \begin{bmatrix} \dot{q}_d \\ \dot{v}_d \\ \dot{w}_d \end{bmatrix} + K_3 \left(\begin{bmatrix} q_d \\ v_d \\ w_d \end{bmatrix} - \begin{bmatrix} q \\ v \\ w \end{bmatrix} \right), \\[12pt]
\boldsymbol{u}_d = \begin{bmatrix} M_{dy} \\ F_{dx} \\ F_{dz} \end{bmatrix} = \begin{bmatrix} I_{yy}\dot{q}_r \\ m(\dot{v}_r + qw + g\sin\theta) \\ m(\dot{w}_r - qv - g\cos\theta) \end{bmatrix}.
\end{cases} \tag{23}$$

The variables with a subscript "d" represent the desired states, and with a subscript "e" represent the value relative to the ground coordinate; for example, θ_d and h_d denote the desired pitch angle and altitude, v_{ed} and w_{ed} denote the ground speed at x and z axis. Additionally, K_1, K_2, and K_3 are positive constants, and R_b^e represents the rotation matrix from the ground coordinate $\mathcal{F}_e$ The optimization results, presented in Table 3, and corresponding to test 1 as depicted in Fig. 7, employ weights w_1, w_2, w_3 as per Eq. , and set up to test the effectiveness of the optimization. The optimization demonstrates an enhanced gust rejection capability for the aircraft, capable of withstanding up to 24 m/s gusts during the tested period.

Different weights w_1, w_2, w_3 in Eq. (20) have been used in the optimization and the gust rejection ability is relatively stable, as presented in Table 3. The optimization demonstrates an enhanced gust rejection capability for the aircraft, capable of withstanding up to 24 m/s gusts during the tested period. The optimized transition trajectory with weights in Test 1, along with its control points, is shown in Fig. 7. The optimized trajectory illustrates the characteristics to first introduce a slight drop to increase the speed, followed by the gradual leaning towards the level flight trim conditions. The altitude increases in this process, with an overshot to settle to its final regions.
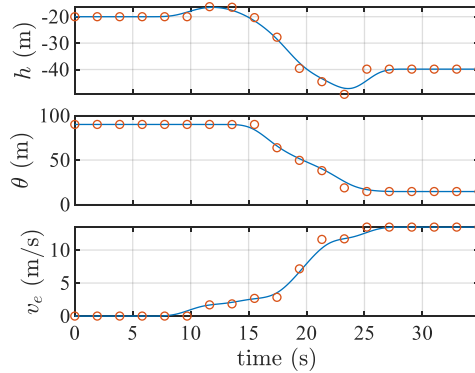
Fig. 7 Optimized ETS-20 transition trajectories of height h, pitch θ, and ground speed v_e

Table 3 Trajectory optimization results with different test setup

Test	w_1	w_2	w_3	Gust rejection ability
Reference	~	~	~	15 m/s (Level 7)
1	1	0.5	1	24 m/s (Level 9)
2	2	0.5	1	24 m/s (Level 9)
3	3	0.5	1	24 m/s (Level 9)

C. Trajectory verification

To further verify the effectiveness of the method, the optimized trajectory is tested in simulation environment with different levels of gust introduced ($0\,\mathrm{m/s}$, $15\,\mathrm{m/s}$, and $24\,\mathrm{m/s}$). It is also compared with an S-shape reference trajectory which connects the given initial and ending condition during the transition with constrained velocity, acceleration, and jerk ($0.5\,\mathrm{m/s}$, $1.2\,\mathrm{m/s^2}$, and $0.2\,\mathrm{m/s^3}$).

Fig. 8 contrasts the optimized trajectory with the reference trajectory under a 24 m/s Von Karman gust. The reference trajectory's performance deteriorates during the transition phase due to the gust, whereas the optimized trajectory maintains stability throughout both the transition and the level flight phases. Notably, as illustrated in Fig. 9, the disturbance impacts the aircraft more during level flight, where lift from the wings and the elevator's action are predominant. Thus, the optimization process not only selects a superior transition trajectory but also establishes a more robust condition for the remainder of the flight. This rationale leads us to utilize a free-end condition, leaving the decision to the optimization process.
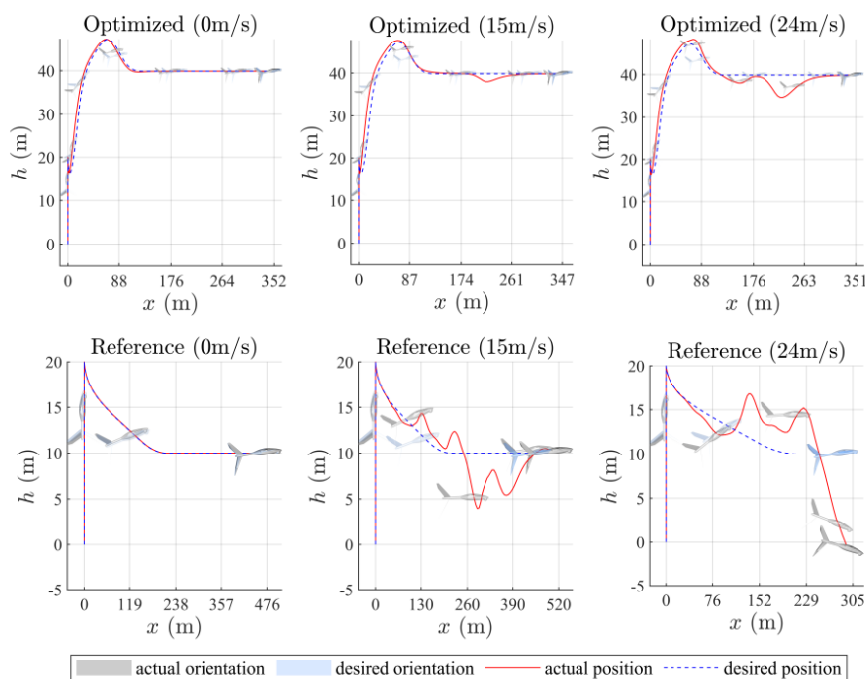
Fig. 8 Aircraft position compare under 0m/s, 15m/s, and 24m/s gust
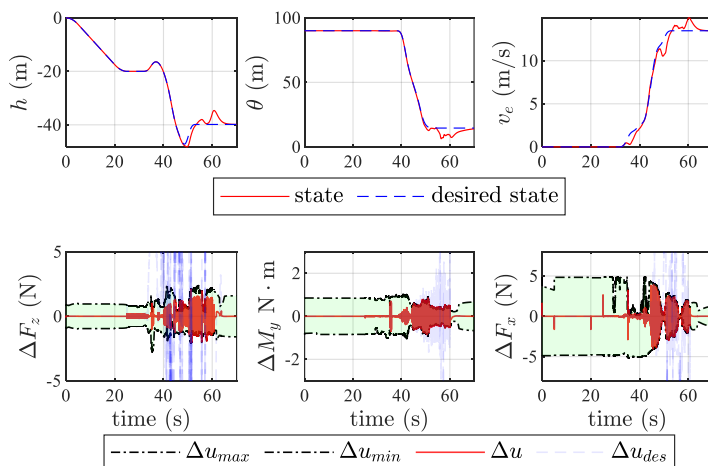
Fig. 9 Aircraft height, pitch, ground speed, and attainable subset under 24 m/s Von Karman gust

IV. Conclusion

This study has demonstrated the development and implementation of a wind resistant transition trajectory optimization for vertical takeoff and landing aircraft within a control allocation framework by calculating the overflow region considering a high level of gust. By defining the overflow region as an indicator of disturbance rejection capability, the trajectory generation problem is converted into an optimizable problem, which is further parameterized with B-spline. The proposed method is verified in simulation on an ETS-20 tail-sitter vertical takeoff and landing aircraft with Von Karman gust model introduced as disturbance. In contrast to a reference S-shape trajectory, the proposed trajectory enhances the gust rejection speed from 15 m/s to 24 m/s. The results obtained from simulation studies lay the groundwork for future study, the next step is to validate these findings through experiments on an experimental platform.

References

[1] Valavanis, Kimon P., ed. "Advances in unmanned aerial vehicles: state of the art and the road to autonomy." (2008).

[2] Jung, Yeunduk, and David Hyunchul Shim. "Development and application of controller for transition flight of tail-sitter UAV." *Journal of Intelligent & Robotic Systems* 65.1-4 (2012): 137-152.

[3] Li, Zhaoying, et al. "Nonlinear robust control of tail-sitter aircrafts in flight mode transitions." *Aerospace Science and Technology* 81 (2018): 348-361.

[4] Yang, Yunjie, Jihong Zhu, and Jiali Yang. "INDI-based transitional flight control and stability analysis of a tail-sitter UAV." 2020 IEEE International Conference on Systems, Man, and Cybernetics (SMC). IEEE, 2020.

[5] Matsumoto, Takaaki, et al. "A hovering control strategy for a tail-sitter VTOL UAV that increases stability against large disturbance." 2010 IEEE international conference on robotics and automation. IEEE, 2010.

[6] Durham, Wayne, Kenneth A. Bordignon, and Roger Beck. *Aircraft control allocation*. John Wiley & Sons, 2017.

[7] Banazadeh, Afshin, Nima Assadian, and Fariborz Saghafi. "Minimum time trajectory optimization of a tail-sitter aerial vehicle using nonlinear programming." The 2012 International Conference on Advanced Mechatronic Systems. IEEE, 2012.

[8] Banazadeh, Afshin, and Neda Taymourtash. "Optimal control of an aerial tail sitter in transition flight phases." *Journal of Aircraft* 53.4 (2016): 914-921.

[9] Verling, Sebastian, et al. "Model-based transition optimization for a VTOL tailsitter." 2017 IEEE International Conference on Robotics and Automation (ICRA). IEEE, 2017.

[10] Naldi, Roberto, and Lorenzo Marconi. "Optimal transition maneuvers for a class of V/STOL aircraft." *Automatica* 47.5 (2011): 870-879.

[11] Hansen, John H., et al. "Control allocation for maneuver and gust load alleviation of flexible aircraft." AIAA Scitech 2020 Forum. 2020.

[12] Oppenheimer, Michael W., David B. Doman, and Michael A. Bolender. "Control allocation for over-actuated systems." 2006 14th Mediterranean Conference on Control and Automation. IEEE, 2006.

[13] Chen, Siqi, et al. "In-situ additive manufacturing deposition trajectory monitoring and compensation with thermal camera." *Additive Manufacturing* 78 (2023): 103820.

[14] Duan, Molong, and Shuaiyin He. "Continuous Fiber Path Optimization in Composite Additive Manufacturing via a Finite Element Model With B-Spline Fiber Parameterization." International Manufacturing Science and Engineering Conference. American Society of Mechanical Engineers, 2023.

[15] Liang, Yu, et al. "Propeller Installation Effect and Surrogate Based Optimization of a Tail-sitter Drone." AIAA AVIATION 2022 Forum. 2022.